

Characterization of a two-transmon processor with individual single-shot qubit readout

A. Dewes¹, F. R. Ong¹, V. Schmitt¹, R. Lauro¹, N. Boulant², P. Bertet¹, D. Vion¹, and D. Esteve¹

¹*Quantronics group, Service de Physique de l'État Condensé (CNRS URA 2464), IRAMIS, DSM, CEA-Saclay, 91191 Gif-sur-Yvette, France and*

²*LRMN, Neurospin, I2BM, DSV, 91191 CEA-Saclay, 91191 Gif-sur-Yvette, France*

(Dated: September 26, 2011)

We report the characterization of a two-qubit processor implemented with two capacitively coupled tunable superconducting qubits of the transmon type, each qubit having its own non-destructive single-shot readout. The fixed capacitive coupling yields the \sqrt{iSWAP} two-qubit gate for a suitable interaction time. We reconstruct by state tomography the coherent dynamics of the two-bit register as a function of the interaction time, observe a violation of the Bell inequality by 22 standard deviations after correcting readout errors, and measure by quantum process tomography a gate fidelity of 90%.

Quantum information processing is one of the most appealing ideas for exploiting the resources of quantum physics and performing tasks beyond the reach of classical machines [1]. Ideally, a quantum processor consists of an ensemble of highly coherent two-level systems, the qubits, that can be efficiently reset, that can follow any unitary evolution needed by an algorithm using a universal set of single and two qubit gates, and that can be readout projectively. In the domain of electrical quantum circuits [2], important progress [3–7] has been achieved recently with the operation of elementary quantum processors based on different superconducting qubits. Those based on transmon qubits [3, 4, 8, 9] are well protected against decoherence but embed all the qubits in a single resonator used both for coupling them and for joint readout. Consequently, individual readout of the qubits is not possible and the results of a calculation, as the Grover search algorithm demonstrated on two qubits [3], cannot be obtained by running the algorithm only once. Furthermore, the overhead for getting a result from such a processor without single-shot readout but with a larger number of qubits overcomes the speed-up gain expected for any useful algorithm. The situation is different for processors based on phase qubits [5, 6, 11], where the qubits are more sensitive to decoherence but can be read individually with high fidelity, although destructively. This significant departure from the wished scheme can be circumvented, when needed, since a destructive readout can be transformed into a non-destructive one at the cost of adding one ancilla qubit and one extra two-qubit gate for each qubit to be read projectively. Moreover, energy release during a destructive readout can result in a sizeable cross-talk between the readout outcomes, which can also be solved at the expense of a more complex architecture [10, 11].

In this work, we operate a new architecture that comes closer to the ideal quantum processor design than the above-mentioned ones. Our circuit is based on frequency tunable transmons that are capacitively coupled. Although the coupling is fixed, the interaction is effective only when the qubits are on resonance, which yields the \sqrt{iSWAP} universal gate for an adequate coupling dura-

tion. Each qubit is equipped with its own non-destructive single-shot readout [12, 13] and the two qubits can be read with low cross-talk. In order to characterize the circuit operation, we reconstruct the time evolution of the two-qubit register density matrix during the resonant and coherent exchange of a single quantum of excitation between the qubits by quantum state tomography. Then, we prepare a Bell state with concurrence 0.85, measure the CHSH entanglement witness, and find a violation of the corresponding Bell inequality by 22 standard deviations. We then characterize the \sqrt{iSWAP} universal gate operation by determining its process map with quantum process tomography [1]. We find a gate fidelity of 90% due to qubit decoherence and systematic unitary errors.

The circuit implemented is schematized in Fig.1a: the coupled qubits with their respective control and readout sub-circuits are fabricated on a Si chip (see supplementary information S1). The chip is cooled down to 20 mK in a dilution refrigerator and connected to room temperature sources and measurement devices by attenuated and filtered control lines and by two measurement lines equipped with cryogenic amplifiers. Each transmon $j = I, II$ is a capacitively shunted SQUID characterized by its Coulomb energy E_C^j for a Cooper pair, the asymmetry d_j between its two Josephson junctions, and its total effective Josephson energy $E_J^j(\phi_j) = E_J^j |\cos(x_j)| \sqrt{1 + d_j^2 \tan^2(x_j)}$, with $x_j = \pi\phi_j/\phi_0$, ϕ_0 the flux quantum, and ϕ_j the magnetic flux through the SQUIDs induced by two local current lines with a 0.5 GHz bandwidth. The transition frequencies $\nu_j \simeq \sqrt{2E_C^j E_J^j}/h$ between the two lowest energy states $|0\rangle_j$ and $|1\rangle_j$ can thus be tuned by ϕ_j . The qubits are coupled by a capacitor with nominal value $C_c \simeq 0.13$ fF and form a register with Hamiltonian $H = h(-\nu_I \sigma_z^I - \nu_{II} \sigma_z^{II} + 2g \sigma_y^I \sigma_y^{II})/2$. Here h is the Planck constant, $\sigma_{x,y,z}$ are the Pauli operators, $2g = \sqrt{E_C^I E_C^{II} \nu_I \nu_{II}}/E_{C_c} \ll \nu_{I,II}$ is the coupling frequency, and E_{C_c} the Coulomb energy of a Cooper pair on the coupling capacitor. The two-qubit gate is defined in the uncoupled basis $\{|uv\rangle\} \equiv \{|0\rangle_I, |1\rangle_I\} \otimes \{|0\rangle_{II}, |1\rangle_{II}\}$,

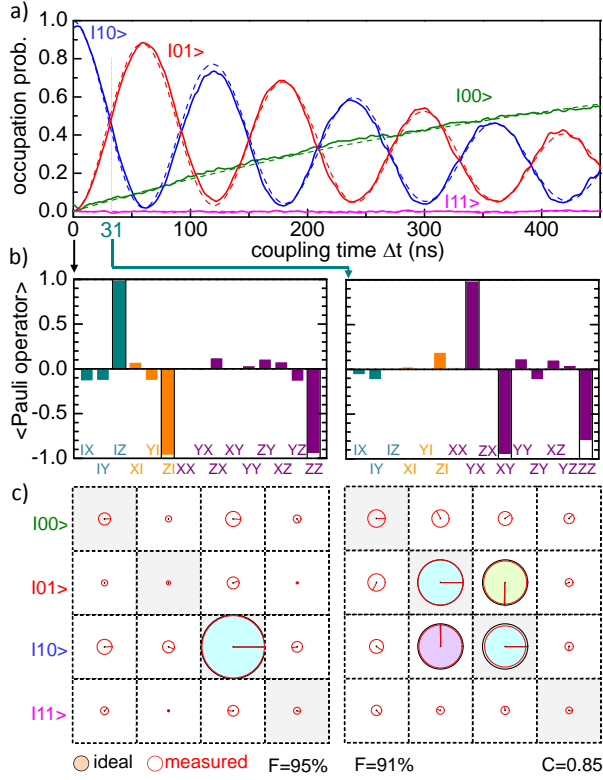


Figure 2: Coherent swapping of a single excitation between the qubits. (a) Experimental (solid lines) and fitted (dashed lines) occupation probabilities of the four computational states $|00\rangle \dots |11\rangle$ as a function of the coupling duration. No Z or tomographic pulses are applied here. (b,c) State tomography of the initial state (left) and of the state produced by the $\sqrt{i}SWAP$ gate (right). (b) Ideal (empty bars) and experimental (color filling) expected values of the 15 Pauli operators XI, \dots, ZZ . (c) Corresponding ideal (color filled black circles with pointer) and experimental (red circle and pointer) density matrices, as well as fidelity F and concurrence C . Each matrix element is represented by a circle with an area proportional to its modulus (diameter = cell size for unit modulus) and a phase pointer giving its argument.

the register density matrix ρ is obtained by measuring the expectation values of the 15 two-qubit Pauli operators $\{P_k\} = \{XI, \dots, ZZ\}$, the X_j and Y_j measurements being obtained using tomographic pulses $\vec{Y}_j(-90^\circ)$ or $\vec{X}_j(90^\circ)$ just before readout. The ρ matrix is calculated from the Pauli set by global minimization of the Hilbert-Schmidt distance between the possibly non-physical ρ and all physical (i.e. positive-semidefinite) ρ' s. This can be done at regular interval of the coupling time to produce a movie of $\rho(\Delta t)$ (see supplementary on line material) showing the swapping of the $|10\rangle$ and $|01\rangle$ populations at frequency $2g$, the corresponding oscillation of the coherences, as well as the relaxation towards $|00\rangle$. Figure 2 shows $\{\langle P_k \rangle\}$ and ρ only at $\Delta t=0$ ns and after a $\sqrt{i}SWAP$ obtained at $\Delta t=31$ ns with Θ_j^{-1} rotations of $\theta_I \simeq -65^\circ$ and $\theta_{II} \simeq +60^\circ$. The fidelity $F = \langle \psi_{id} | \rho | \psi_{id} \rangle$

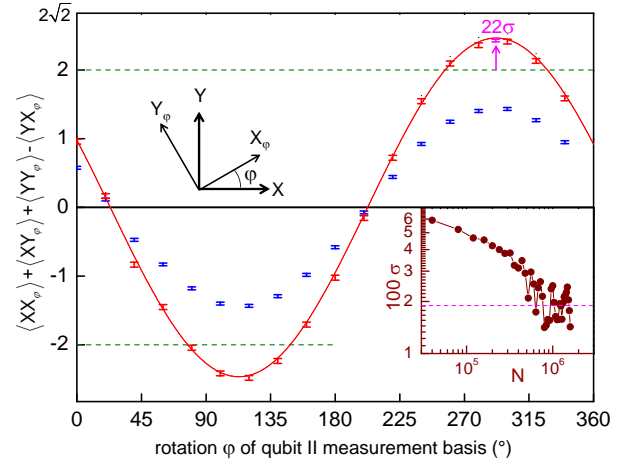


Figure 3: Test of the CHSH-Bell inequality on a $|10\rangle + e^{i\psi}|01\rangle$ state by measuring the qubits along X^I or Y^I and X_φ^{II} or Y_φ^{II} (see top-left inset), respectively. Blue (resp. red) error bars are the experimental CHSH entanglement witness determined from the raw (resp. readout errors corrected) measurements as a function of the angle φ between the measuring basis, whereas solid line is a fit using ψ as the only fitting parameter. Height of error bars is \pm one standard deviation $\sigma(N)$ (see bottom-right inset), with N the number of sequences per point. Note that averaging beyond $N = 10^6$ does not improve the violation because of a slow drift of φ .

of ρ with the ideal density matrices $|\psi_{id}\rangle \langle \psi_{id}|$ are 95% and 91%, respectively, and are limited by errors on the preparation pulse, statistical noise, and relaxation.

To quantify in a different way our ability to entangle the two qubits, we prepare a Bell state $|10\rangle + e^{i\psi}|01\rangle$ (with $\psi = \theta_{II} - \theta_I$) using the pulse sequence of Fig. 1c with $\Delta t = 31$ ns and no Θ_j^{-1} rotations, and measure the CHSH entanglement witness $\langle XX_\varphi \rangle + \langle XY_\varphi \rangle + \langle YY_\varphi \rangle - \langle YX_\varphi \rangle$ as a function of the angle φ between the orthogonal measurement bases of qubit I and II . Figure 3 compares the results obtained with and without correcting the readout errors, with what is theoretically expected from the decoherence parameters indicated previously: unlike in [10] and because of a readout contrast limited to 70 – 75 %, the witness does not exceed the classical bound of 2 without correcting the readout errors. After correction, it reaches 2.43, in good agreement with the theoretical prediction (see also [14]), and exceeds the classical bound by up to 22 standard deviations when averaged over 10^6 sequences.

In a last experiment, we characterize the imperfections of our $\sqrt{i}SWAP$ gate by quantum process tomography [1]. We build a completely positive map $\rho_{out} = \mathcal{E}(\rho_{in}) = \sum_{m,n} \chi_{mn} P'_m \rho_{in} P'_n{}^\dagger$ characterized by a 16×16 matrix χ expressed here in the modified Pauli operator basis $\{P'_k\} = \{I, X, Y' = iY, Z\}^{\otimes 2}$, for which all matrices are real. For that purpose, we apply the gate (using pulse sequences similar to that of 1c, with $\Delta t = 31$ ns and Θ_j^{-1} rotations) to the sixteen input states

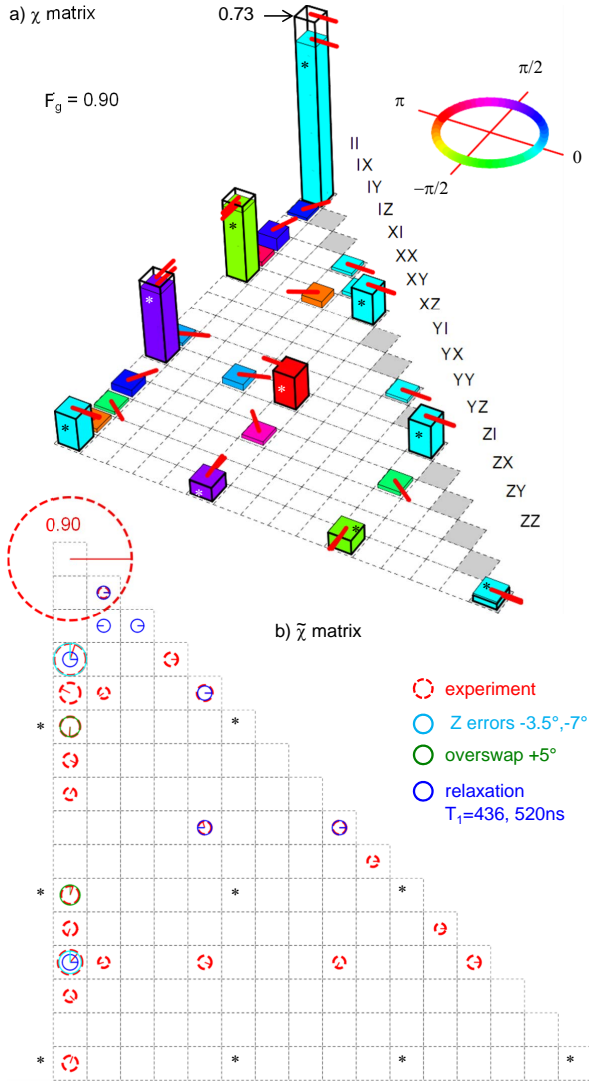


Figure 4: Map of the implemented $\sqrt{i}\text{SWAP}$ gate yielding a fidelity of 90%. (a) Superposition of the ideal (empty thick bars) and experimental (color filled bars) lower part of the Hermitian matrix χ (elements below 1% not shown). Each complex matrix element is represented by a bar with height proportional to its modulus and a red phase pointer at the top of the bar (as well as a filling color for experiment) giving its argument (top left inset). Expected peaks are marked by a star. (b) Lower part of the $\tilde{\chi}$ error matrix (red circles - see text), with the same convention as in Fig.2, but with circles magnified for readability (a one-cell diameter represents a 8 % modulus). Main visible contributions (continuous circles) are explained in text.

$\{|0\rangle, |1\rangle, |0\rangle + |1\rangle, |0\rangle + i|1\rangle\}^{\otimes 2}$ and characterize both the input and output states by quantum state tomography. By operating as described previously, we would obtain apparent input and output density matrices including errors made in the state tomography itself, which we don't want to include in the gate map. Instead, we fit the 16 experimental input Pauli sets by a model including amplitude and phase errors for the X and Y preparation and tomographic pulses (see S4), in order to determine which operator set $\{P_k^e\}$ is actually measured. The input and output matrices $\rho_{\text{in,out}}$ corrected from the tomographic errors only are calculated by inverting the linear relation $\{\langle P_k^e \rangle = \text{Tr}(\rho P_k^e)\}$ and by applying it to the experimental Pauli sets. We then calculate from the $\{\rho_{\text{in,out}}\}$ set an Hermitian χ matrix that is not necessarily physical due to statistical errors, and which we render physical by taking the nearest Hermitian positive matrix. This final χ matrix is shown in Fig. 4 and compared to the ideal one, χ_{id} , which yields a gate fidelity $F_g = \text{Tr}(\chi \cdot \chi_{\text{id}}) = 0.9$ [15]. To better understand the imperfections, we also show the map $\tilde{\chi}$ of the actual process preceded by the inverse ideal process [16]. The first diagonal element of $\tilde{\chi}$ is equal to F by construction. Then, main visible errors arise from unitary operations and reduce fidelity by 1-2% (a fit yields a too long coupling time inducing a 95° swap instead of 90° and $\Theta_{1,2}$ rotations too small by 3.5° and 7° respectively). On the other hand the known relaxation and dephasing times reduces fidelity by 8% but is barely visible in $\tilde{\chi}$ due to a spread over many matrix elements with modulus of the order of or below the 1 – 2% noise level.

As a conclusion, we have demonstrated a high fidelity $\sqrt{i}\text{SWAP}$ gate in a two josephson qubit circuit with individual non-destructive single-shot readouts, observed a violation of the CHSH-Bell inequality, and followed the register's dynamics by tomography. Although quantum coherence and readout fidelity are still limited in this circuit, they are sufficient to test in the near future simple quantum algorithms and get their result in a single run, which would demonstrate the concept of quantum speed-up.

We gratefully acknowledge discussions with J. Martinis and his coworkers, with M. Devoret, D. DiVicenzo, A. Korotkov, P. Milman, and within the Qunatronics group, technical support from P. Orfila, P. Senat, and J.C. Tack, as well as financial support from the European research contracts MIDAS and SOLID, from ANR Masquelspec and C'Nano and from the German Ministry of Education and Research.

[1] M. A. Nielsen and I. L. Chuang, Quantum Computation and Quantum Information (Cambridge University Press, Cambridge, UK, 2000).
 [2] J. Clarke and F. Wilhelm, Nature **453**, 1031 (2008).

[3] L. DiCarlo *et al.*, Nature **460**, 240 (2008).
 [4] L. DiCarlo *et al.*, Nature **467**, 574 (2010).
 [5] T. Yamamoto *et al.*, Phys. Rev. B **82**, 184515 (2010).
 [6] R. C. Bialczak *et al.*, Nature Physics **6**, 409-413 (2010).

- [7] J. M. Chow *et al.*, Phys. Rev. Lett. **107**, 080502 (2011).
- [8] J. Koch *et al.*, Phys. Rev. A **76**, 042319 (2007).
- [9] J.A. Schreier *et al.*, Phys. Rev. B **77**, 180502(R) (2008).
- [10] M. Ansmann *et al.*, Nature **461**, 504 (2009).
- [11] M. Mariani *et al.*, Science, DOI: 10.1126/science.1208517 (2011).
- [12] I. Siddiqi *et al.*, Phys. Rev. Lett. **93**, 207002 (2004).
- [13] F. Mallet *et al.*, Nature Physics **5**, 791 (2009).
- [14] J. M. Chow *et al.*, Phys. Rev. A **81**, 062325 (2010).
- [15] Note that F_g is also equal to Shumacher's fidelity $Tr[S_{id}^\dagger S]/Tr[S_{id}^\dagger S_{id}]$ with S (resp. S_{id}) the super operator of the actual (resp. ideal unitary) process, and that fidelities F for the 16 outputs states range between 80% and 99.5%
- [16] A. G. Kofman and A. N. Korotkov, Phys. Rev. A, vol. **81**, no. 4, 042103 (2009), and private communication.

Supplementary Information for Characterization of a two-transmon processor with individual single-shot qubit readout

A. Dewes¹, F. R. Ong¹, V. Schmitt¹, R. Lauro¹, N. Boulant², P. Bertet¹, D. Vion¹, and D. Esteve¹

¹ *Quantronics group, Service de Physique de l'État Condensé (CNRS URA 2464),*

IRAMIS, DSM, CEA-Saclay, 91191 Gif-sur-Yvette, France and

² *I2BM, Neurospin, LRMN, 91191 CEA-Saclay, 91191 Gif-sur-Yvette, France*

(Dated: September 26, 2011)

S1. Sample preparation

The sample is fabricated on a silicon chip oxidized over 50 nm. A 150 nm thick niobium layer is first deposited by magnetron sputtering and then dry-etched in a SF_6 plasma to pattern the readout resonators, the current lines for frequency tuning, and their ports. Finally, the transmon qubit, the coupling capacitance and the Josephson junctions of the resonators are fabricated by double-angle evaporation of aluminum through a shadow mask patterned by e-beam lithography. The first layer of aluminum is oxidized in a $Ar - O_2$ mixture to form the oxide barrier of the junctions. The chip is glued with wax on a printed circuit board (PCB) and wire bonded to it. The PCB is then screwed in a copper box anchored to the cold plate of a dilution refrigerator.

S2. Sample parameters

The sample is first characterized by spectroscopy (see Fig. 1.b of main text). The incident power used is high enough to observe the resonator frequency ν_R , the qubit line ν_{01} , and the two-photon transition at frequency $\nu_{02}/2$ between the ground and second excited states of each transmon (data not shown). A fit of the transmon model to the data yields the sample parameters $E_J^I/h = 36.2$ GHz, $E_C^I/h = 0.98$ GHz, $d_I = 0.2$, $E_J^{II}/h = 43.1$ GHz, $E_C^{II}/h = 0.87$ GHz, $d_{II} = 0.35$, $\nu_R^I = 6.84$ GHz, and $\nu_R^{II} = 6.70$ GHz. The qubit-readout anticrossing at $\nu = \nu_R$ yields the qubit-readout couplings $g_0^I \simeq g_0^{II} \simeq 50$ MHz. Independent measurements of the resonator dynamics (data not shown) yield quality factors $Q_I = Q_{II} = 730$ and Kerr non linearities [13,[1]] $K_I/\nu_R^I \simeq K_{II}/\nu_R^{II} \simeq -2.3 \pm 0.5 \times 10^{-5}$.

S3. Experimental setup

- **Qubit microwave pulses:** The qubit drive pulses are generated by two phase-locked microwave generators whose continuous wave outputs are fed to a pair of I/Q-mixers. The two IF inputs of each of these mixers are provided by a 4-Channel 1 GS/s arbitrary waveform generator (AWG Tektronix AWG5014). Single-sideband mixing in the frequency range of 50-300 MHz is used to generate multi-tone drive pulses and to obtain a high ON/OFF ratio (> 50 dB) of the signal at the output of the mixers. Phase and amplitude errors of the mixers are corrected by measuring the signals at the output and applying sideband and carrier frequency dependent corrections in amplitude and offset to the IF input channels.
- **Flux Pulses:** The flux control pulses are generated by a second AWG and sent to the chip through a transmission line, equipped with 40 dB of attenuation distributed over different temperature stages and a pair of 1 GHz absorptive low-pass filters at 4 K. The input signal of each flux line is fed back to room temperature through an identical transmission line and measured to compensate the non-ideal frequency response of the line.
- **Readout Pulses:** The pulses for the Josephson bifurcation amplifier (JBA) readouts are generated by mixing the continuous signals of a pair of microwave generators with IF pulses provided by a 1 GS/s arbitrary function generator. Each readout pulse consists of a measurement part with a rise time of 30 ns and a hold time of 100 ns, followed by a $2 \mu s$ long latching part at 90 % of the pulse height.
- **Drive and Measurement Lines:** The drive and readout microwave signals of each qubit are combined and sent to the sample through a pair of transmission lines that are attenuated by 70 dB over different temperature stages and filtered at 4 K and 300 mK. A microwave circulator at 20 mK separates the input signals going to the chip from the reflected signals coming from the chip. The latter are amplified by 36 dB at 4 K by two cryogenic HEMT amplifiers (CIT Cryo 1) with noise temperature 5 K. The reflected readout pulses get further amplified at room temperature and demodulated with the continuous signals of the readout microwave sources. The IQ quadratures of the demodulated signals are sampled at 1 GS/s by a 4-channel Data Acquisition system (Acqiris DC282).

S4. Readout characterization

Errors in our readout scheme are discussed in detail in [13] for a single qubit. First, incorrect mapping $|0\rangle \rightarrow 1$ or $|1\rangle \rightarrow 0$ of the projected state of the qubit to the dynamical state of the resonator can occur, due to the stochastic nature of the switching between the two dynamical states. As shown in Fig. S4.1, the probability p to obtain the outcome 1 varies continuously from 0 to 1 over a certain range of drive power P_d applied to the readout. When the shift in power between the two $p_{|0\rangle,|1\rangle}(P_d)$ curves is not much larger than this range, the two curves overlap and errors are significant even at the optimal drive power where the difference in p is maximum. Second, even in the case of non overlapping $p_{|0\rangle,|1\rangle}(P_d)$ curves, the qubit initially projected in state $|1\rangle$ can relax down to $|0\rangle$ before the end of the measurement, yielding an outcome 0 instead of 1. The probability of these two types of errors vary in opposite directions as a function of the frequency detuning $\Delta = \nu_R - \nu > 0$ between the resonator and the qubit, so that a compromise has to be found for Δ . Besides, the contrast $c = \text{Max}(p_{|1\rangle} - p_{|0\rangle})$ can be increased [12] by shelving state $|1\rangle$ into state $|2\rangle$ with a microwave π pulse at frequency ν_{12} just before the readout resonator pulse. The smallest errors $e_0^{\text{I,II}}$ and $e_1^{\text{I,II}}$ when reading $|0\rangle$ and $|1\rangle$ are found for $\Delta_{\text{I}} = 440$ MHz and $\Delta_{\text{II}} = 575$ MHz and are shown by arrows in the top panels of Fig. S3.2: $e_0^{\text{I}} = 5\%$ and $e_1^{\text{I}} = 13\%$ (contrast $c_{\text{I}} = 1 - e_0^{\text{I}} - e_1^{\text{I}} = 82\%$), and $e_0^{\text{II}} = 5.5\%$ and $e_1^{\text{II}} = 12\%$ ($c_{\text{II}} = 82\%$). When using the $|1\rangle \rightarrow |2\rangle$ shelving before readout, $e_0^{\text{I}} = 2.5\%$ and $e_2^{\text{I}} = 9.5\%$ (contrast $c_{\text{I}} = 1 - e_0^{\text{I}} - e_2^{\text{I}} = 88\%$), and $e_0^{\text{II}} = 3\%$ and $e_2^{\text{II}} = 8\%$ ($c_{\text{II}} = 89\%$). These best results are very close to those obtained in [12], but are unfortunately not relevant to this work.

Indeed, when the two qubits are measured simultaneously, one has also to take into account a possible readout crosstalk, i.e. an influence of the projected state of each qubit on the outcome of the readout of the other qubit. We do observe such an effect and have to minimize it by increasing $\Delta_{\text{I,II}}$ up to ~ 1 GHz with respect to previous optimal values and by not using the shelving technique. An immediate consequence shown in Fig. 3.2 (b) is a reduction of the $c_{\text{I,II}}$ contrasts. The errors when reading $|0\rangle$ and $|1\rangle$ are now $e_0^{\text{I}} = 19\%$ and $e_1^{\text{I}} = 7\%$ (contrast $c_{\text{I}} = 74\%$) and $e_0^{\text{II}} = 19\%$ and $e_1^{\text{II}} = 12\%$ (contrast $c_{\text{II}} = 69\%$). Then to characterize the errors due to crosstalk, we measure the 4×4 readout matrix \mathcal{R} linking the probabilities p_{uv} of the four possible uv outcomes to the population of the four $|uv\rangle$ states. As shown in Fig. S3.2(c-d), we then rewrite $\mathcal{R} = \mathcal{C}_{\text{CT}} \cdot (\mathcal{C}_{\text{I}} \otimes \mathcal{C}_{\text{II}})$ as the product of a 4×4 pure crosstalk matrix \mathcal{C}_{CT} with the tensorial product of the two 2×2 single qubit readout matrices

$$\mathcal{C}_{\text{I,II}} = \begin{pmatrix} 1 - e_0^{\text{I,II}} & e_1^{\text{I,II}} \\ e_0^{\text{I,II}} & 1 - e_1^{\text{I,II}} \end{pmatrix}.$$

We also illustrate on the figure the impact of the readout errors on our swapping experiment by comparing the bare readout outcomes uv , the outcomes corrected from the independent readout errors only, and the $|uv\rangle$ population calculated with the full correction including crosstalk.

We now explain briefly the cause of the readout crosstalk in our processor. Unlike what was observed for other qubit readout schemes using switching detectors [5], the crosstalk we observe is not directly due to an electromagnetic perturbation induced by the switching of one detector that would help or prevent the switching of the other one. Indeed, when both qubits frequencies $\nu_{\text{I,II}}$ are moved far below $\nu_{\text{R}}^{\text{I,II}}$, the readout crosstalk disappears: the switching of a detector has no measurable effect on the switching of the other one. The crosstalk is actually due to the rather strong ac-Stark shift $\sim 2(n_{\text{H}} - n_{\text{L}})g_0^2/(R - \nu_{\text{R}}) \sim 500$ MHz of the qubit frequency when a readout resonator switches from its low to high amplitude dynamical state with $n_{\text{L}} \sim 10$ and $n_{\text{H}} \sim 10^2$ photons, respectively. The small residual effective coupling between the qubits at readout can then slightly shift the frequency of the other resonator, yielding a change of its switching probability by a few percent. Note that coupling the two qubits by a resonator rather than by a fixed capacitor would solve this problem.

S5. Removing errors on tomographic pulses before calculating the gate process map

Tomographic errors are removed from the process map of our $\sqrt{i\text{SWAP}}$ gate using the following method. The measured Pauli sets corresponding to the sixteen input states are first fitted by a model including errors both in the preparation of the state (index *prep*) and in the tomographic pulses (index *tomo*). The errors included are angular errors $\varepsilon_{\text{I,II}}^{\text{prep}}$ on the nominal π rotations around $X_{\text{I,II}}$, $\eta_{\text{I,II}}^{\text{prep,tomo}}$ and $\delta_{\text{I,II}}^{\text{prep,tomo}}$ on the nominal $\pi/2$ rotations around $X_{\text{I,II}}$ and $Y_{\text{I,II}}$, a possible departure $\xi_{\text{I,II}}$ from orthogonality of $(\vec{X}_{\text{I}}, \vec{Y}_{\text{I}})$ and $(\vec{X}_{\text{II}}, \vec{Y}_{\text{II}})$, and a possible rotation $\mu_{\text{I,II}}$ of the tomographic XY frame with respect to the preparation one. The rotation operators used for preparing the states and doing their tomography are thus given by

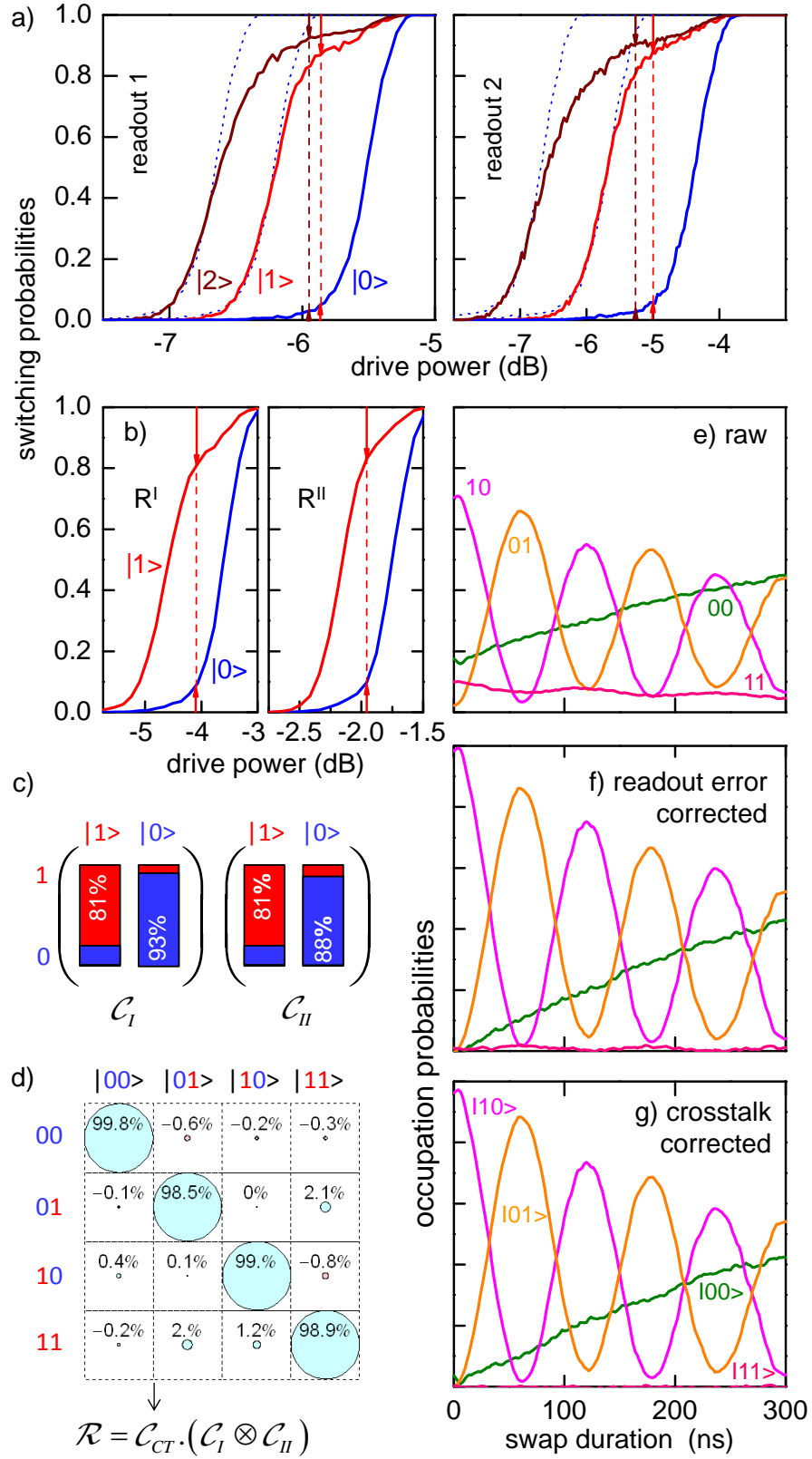


Figure 1: Readout imperfections and their correction. (a) Switching probabilities of the readouts as a function of their driving power, with the qubit prepared in state $|0\rangle$ (blue), $|1\rangle$ (red), or $|2\rangle$ (brown), at the optimal readout points. The arrows and dashed segments indicate the readout errors and contrast, at the power where the latter is maximum. (b) Same as (a) but at readout points $R^{I,II}$ used in this work. (c-d) Single readout matrices $\mathcal{C}_{I,II}$ and pure readout crosstalk matrix \mathcal{C}_{CT} characterizing the simultaneous readout of the two qubits. (e-g) bare readout outcomes uv , outcomes corrected from the independent readout errors only, and $|uv\rangle$ population calculated with the full correction including crosstalk for the swapping experiment of Fig. 2.

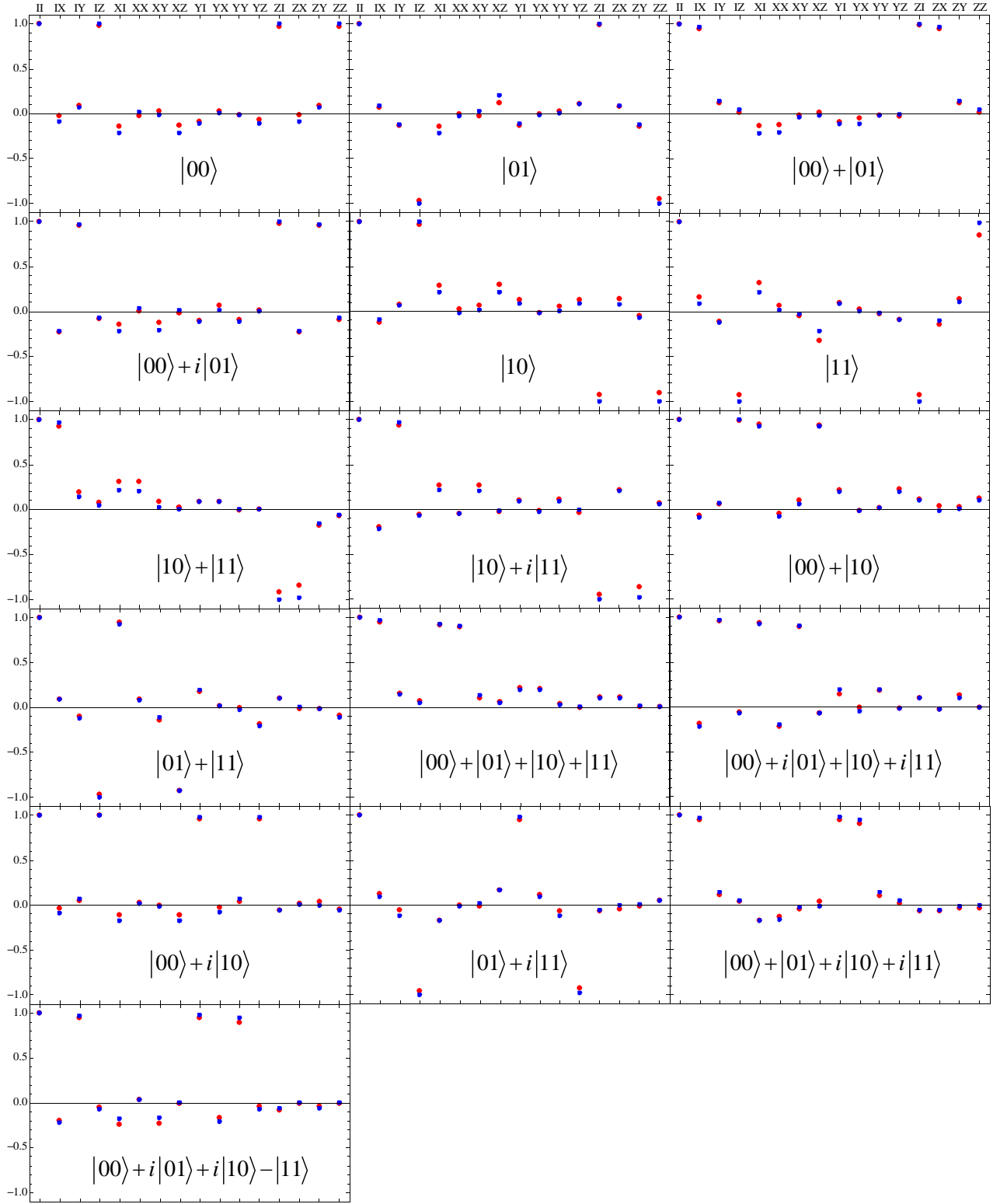


Figure 2: Fitting of the pulse errors at state preparation and tomography. Measured (red) and fitted (blue - see text) Pauli sets $\langle P_k^e \rangle$ for the sixteen targeted input states $\{|0\rangle, |1\rangle, |0\rangle + |1\rangle, |0\rangle + i|1\rangle\}^{\otimes 2}$. The $\{II, IX, IY, IZ, XI, \dots\}$ operators indicated in abscisse are the targeted operators and not those actually measured (due to tomographic errors).

$$\begin{aligned}
X_{I,\Pi}^{\text{prep}}(\pi) &= e^{-i(\pi+\varepsilon_{I,\Pi}^{\text{prep}})\sigma_x^{I,\Pi}/2}, \\
X_{I,\Pi}^{\text{prep}}(-\pi/2) &= e^{+i(\pi/2+\eta_{I,\Pi}^{\text{prep}})\sigma_x^{I,\Pi}/2}, \\
Y_{I,\Pi}^{\text{prep}}(\pi/2) &= e^{-i(\pi/2+\delta_{I,\Pi}^{\text{prep}})[\cos(\xi_{I,\Pi})\sigma_y^{I,\Pi}-\sin(\xi_{I,\Pi})\sigma_x^{I,\Pi}]/2}, \\
X_{I,\Pi}^{\text{tomo}}(\pi/2) &= e^{-i(\pi/2+\eta_{I,\Pi}^{\text{tomo}})[\sin(\mu_{I,\Pi})\sigma_x^{I,\Pi}+\cos(\mu_{I,\Pi})\sigma_y^{I,\Pi}]/2}, \\
Y_{I,\Pi}^{\text{tomo}}(-\pi/2) &= e^{+i(\pi/2+\delta_{I,\Pi}^{\text{tomo}})[\cos(\mu_{I,\Pi}+\xi_{I,\Pi})\sigma_y^{I,\Pi}-\sin(\mu_{I,\Pi}+\xi_{I,\Pi})\sigma_x^{I,\Pi}]/2}.
\end{aligned}$$

The sixteen input states are then $\{\rho_{\text{in}}^e = U|0\rangle\langle 0|U^\dagger\}$ with $\{U\} = \{I_I, X_I^{\text{prep}}(\pi), Y_I^{\text{prep}}(\pi/2), X_I^{\text{prep}}(-\pi/2)\} \otimes \{I_{II}, X_{II}^{\text{prep}}(\pi), Y_{II}^{\text{prep}}(\pi/2), X_{II}^{\text{prep}}(-\pi/2)\}$, and each input state yields a Pauli set $\{\langle P_k^e \rangle = \text{Tr}(\rho_{\text{in}}^e P_k^e)\}$ with $\{P_k^e\} = \{I_I, X_I^e, Y_I^e, Z_I\} \otimes \{I_{II}, X_{II}^e, Y_{II}^e, Z_{II}\}$, $X^e = Y^{\text{tomo}}(-\pi/2)^\dagger \sigma_z Y^{\text{tomo}}(-\pi/2)$, and $Y^e = X^{\text{tomo}}(\pi/2)^\dagger \sigma_z X^{\text{tomo}}(\pi/2)$. Figure S5.1 shows the best fit of the modelled $\{\langle P_k^e \rangle\}$ set to the measured input Pauli sets, yielding $\varepsilon_I^{\text{prep}} = -1^\circ$, $\varepsilon_{II}^{\text{prep}} = -3^\circ$, $\eta_I^{\text{prep}} = 3^\circ$, $\eta_{II}^{\text{prep}} = 4^\circ$, $\delta_I^{\text{prep}} = -6^\circ$, $\delta_{II}^{\text{prep}} = -3^\circ$, $\eta_I^{\text{tomo}} = -6^\circ$, $\eta_{II}^{\text{tomo}} = -4^\circ$, $\lambda_I^{\text{tomo}} = 12^\circ$, $\lambda_{II}^{\text{tomo}} = 5^\circ$, $\xi_I = 1^\circ$, $\xi_{II} = -2^\circ$, and $\mu_I = \mu_{II} = -11^\circ$.

Knowing the tomographic errors and thus $\{\langle P_k^e \rangle\}$, we then invert the linear relation $\{\langle P_k^e \rangle = \text{Tr}(\rho P_k^e)\}$ to find the 16×16 matrix B that links the vector $\overrightarrow{\langle P_k^e \rangle}$ to the columnized density matrix $\overrightarrow{\rho}$, i.e. $\overrightarrow{\rho} = B \cdot \overrightarrow{\langle P_k^e \rangle}$. The matrix B is finally applied to the measured sixteen input and sixteen output Pauli sets to find the sixteen $(\rho_{\text{in}}, \rho_{\text{out}})_k$ couples to be used for calculating the gate map.

[1] F. R. Ong *et al.*, Phys. Rev. Lett. 106, 167002 (2011).

Supplementary Online Material for Characterization of a two-transmon processor with individual single-shot qubit readout

A. Dewes¹, F. R. Ong¹, V. Schmitt¹, R. Lauro¹, N. Boulant², P. Bertet¹, D. Vion¹, and D. Esteve¹

¹*Quantronics group, Service de Physique de l'État Condensé (CNRS URA 2464), IRAMIS, DSM, CEA-Saclay, 91191 Gif-sur-Yvette, France and*

²*I2BM, Neurospin, LRMN, 91191CEA-Saclay, 91191 Gif-sur-Yvette, France*

(Dated: September 26, 2011)

Animated gif file to be included in the supplementary online material.

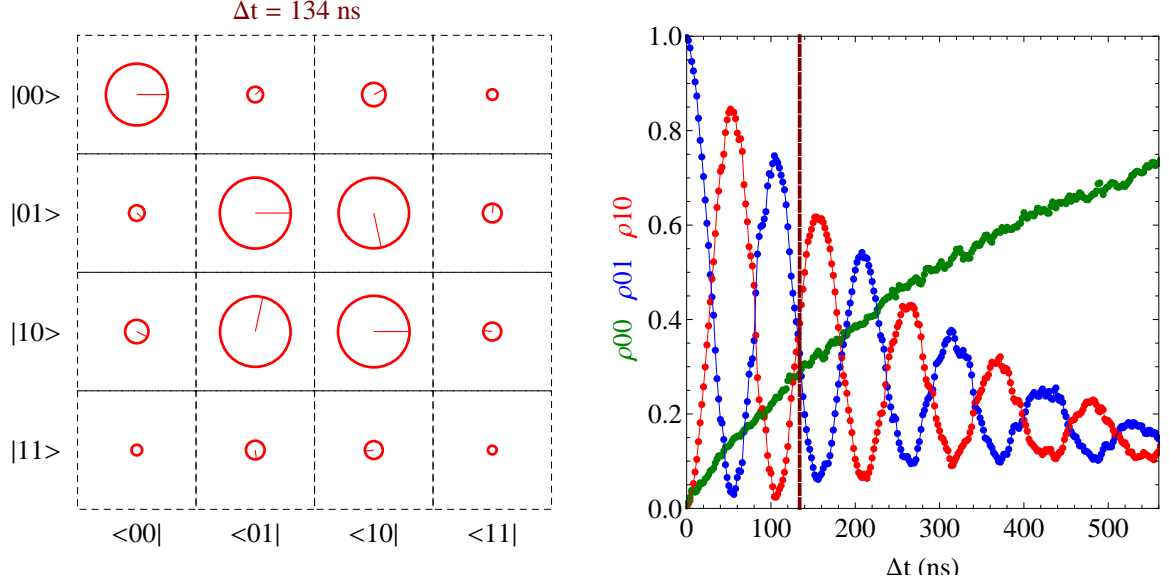


Figure 1: Reconstruction of the two-bit register density matrix by quantum state tomography during the *iSWAP* gate operation. The working point is slightly different from the one reported in Figs 1 and 2 of our Letter. The main characteristics of the dynamics are clearly visible on the animated density matrix shown on the left, where each matrix element is represented by a circle with area proportional to its modulus (unit modulus for a circle touching the cell borders), and in the plot of the populations $\rho_{00} = \rho_{|00\rangle\langle 00|}$, $\rho_{01} = \rho_{|01\rangle\langle 01|}$, and $\rho_{10} = \rho_{|10\rangle\langle 10|}$ (on the right): we observe the swapping of ρ_{00} and ρ_{01} at frequency $2g$, the oscillations of the coherence amplitude $|\rho_{|01\rangle\langle 10||}$ at the double frequency, the fast rotation of its phase $\arg(\rho_{|01\rangle\langle 10|})$, as well as the relaxation towards $|00\rangle$. However, the picture is less quantitative than Fig. 2 due to slow technical drifts that occurred during the several hour long data collection. These drifts are responsible for small uncontrolled rotations of the measured operators, which build spurious coherent matrix elements: one sees for instance $\rho_{|00\rangle\langle 01|}$ unexpectedly peaking at 9% at $\Delta t = 8 \text{ ns}$ and $\rho_{|00\rangle\langle 10|}$ reaching about the same error after 350 ns.